

Fig. 2. LNA and Switch ICs (a) LNA circuit schematic. (b) LNA gain (blue) and Noise Figure (red). (c) Switch schematic. (d) Insertion Loss (top), Cross-channel isolation (middle) and Noise Temperature (bottom) vs frequency. Green (orange) trace typical (worst) case. Typical Noise Temperature (bottom). Measurements performed at 4 K ambient temperature.

oxide flipped-well NMOS devices which have shown excellent RF performance in the deep-cryogenic regime [10]. Figure 2(a) shows the simplified schematic of the LNA IC with additional external passives for input and output matching. We integrated the IC and passives in a PCB module (Fig. 1(a) and (b)), and characterized it at 4 K ambient temperature. Figure 2(b) shows the measurement results. We show a peak S_{21} greater than 35 dB at 780 MHz and a 3dB bandwidth from 709 MHz to 827 MHz, an input-referred average NT of 6.2 K over the LNA bandwidth, and a minimum NT of 4.2 K at 650 MHz, see Fig. 2(b). Note that the noise match happens below the LNA bandwidth due to not accurately modelled changes in the electrical characteristics of the devices in the deep-cryogenic regime. The measured standby power consumption of the module is 36 mW.

CRYOGENIC SP8T SWITCH

To provide cryogenic time-domain RF multiplexing, we designed a SP8T RF switch IC. The IC is comprised of: a digital block, and a RF switch block. The digital block provides external communication using the SPI protocol and generates the control signals for the RF block. The RF block contains eight series-only switching units. The switching units use thick oxide flipped-well NMOS devices operated in dynamic threshold-voltage mode. Figure 2(c) shows the block diagram of the IC including a simplified schematic of the RF block. We integrated the chiplet in a PCB module (Fig. 1(c) and (d)), and characterized it in the 0-2 GHz input frequency range and at 4K ambient temperature (Fig. 2(d)). We show for all channels an insertion loss of less than 1.1 dB, a cross-channel isolation better than 35 dB and a NT smaller than 1.1 K. The measured standby power consumption of the module is below the measurement resolution of 100 nW, and within the cooling budget of the mixing chamber [9]. We functionally validated the module at mK ambient temperature and expect its performance to be comparable to the 4 K measurements [11].

We present results on SEBs charge detectors, (SEB_i for $i = 0, 1$). The devices are implemented in a narrow channel multi-gate transistor, see Fig. 3(a). When a positive potential, near the threshold voltage, is applied to a gate (G_i) placed next to an ohmic contact (RX_i), a QD tunnel-coupled to an electron reservoir forms, i.e a SEB. We probe the impedance of the device using RF transmission techniques by applying an RF excitation to G_i and collecting the transmitted signal on the RX_i port where a sub-1 GHz L-shape high-pass matching resonant network of center frequency f_i is placed [12]. We refer to these matching networks as MN: i , see Fig. 3(b). When electrons cyclically tunnel between the QD and the reservoir due to the RF excitation, a change in the transmission through the device occurs. We perform the measurements on two SEBs at mK ambient temperature as a function of the respective gate voltage, see orange and green traces in Fig. 3(c). Such sharp change in transmission can be used for sensitive charge detection of nearby QDs or qubits [13]. The linewidth of these transitions can be used to provide an upper bound of the electron temperature of the SEBs [14], for which we find 360 mK. We integrated the chiplet in a PCB module (Fig. 1(e) and (f)).

MULTI-MODULE CRYOGENIC ASSEMBLY

Next, we move on to the cryogenic characterisation of the full assembly, see Fig. 4(a). We send an attenuated RF signal to the switch module which acts as a multiplexer (MUX) placed at mixing chamber of a dilution refrigerator with base temperature of 20 mK. The MUX distributes the signal on-demand through channels MUX:0 and MUX:1 to the SEB chiplet also placed at the mixing chamber plate. Then the transmitted signal through each SEBs is impedance-matched at the output using the LC networks. The signal is then amplified by the LNA and base-band IQ demodulated at room temperature.

We now characterize the S-parameters of the assembly, see Fig. 4(b). First, in blue, we plot a S_{12} measurement, equivalent to a RF reflectometry test, showing two sharp resonances at the frequency of the LC resonators (red dashed lines) from which we determine f_i . We now characterize the transmission through the assembly, S_{13} , including the MUX. In orange(green), we activate MUX:0(1) and show the transmission primarily happens through MN:0(1) with an isolation to MN:1(0) of > 13 dB. Additionally, we show measurements when MUX:2,3,7 are active (red, purple and brown lines) indicating a > 39 dB internal MUX isolation. Cross-coupling at the SEB chiplet contributes to the difference in isolation. Finally, in Fig. 4(c), we combine the three modules into a demonstration of multi-frequency time-division multiplexing. We continuously send two RF tones at $f_0 = 559$ MHz and $f_1 = 681$ MHz. First, for $t < 400$ ms, we select MUX:0 and detect the charge oscillations as a function of gate voltage in SEB_0 (see the blue trace in the bottom panel). During this time period, we ramp the gate voltage of SEB_0 (top panel) to change the charge state of the SEB, while the gate voltage on SEB_1

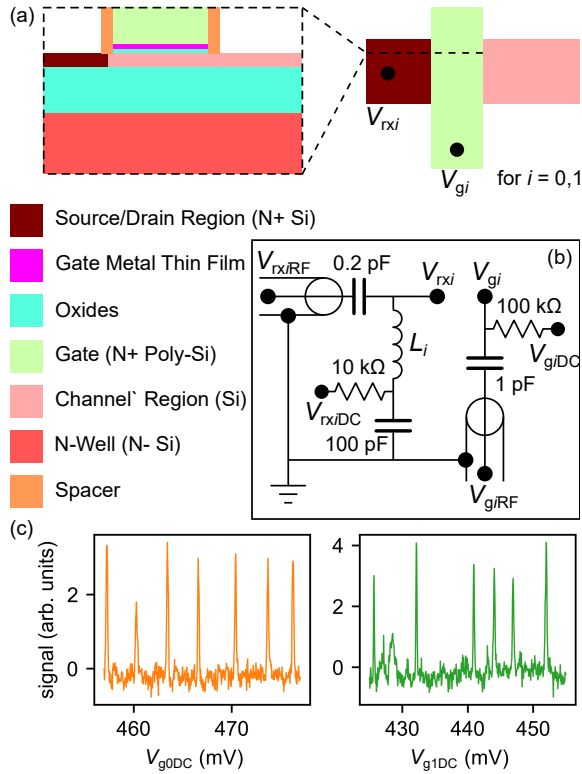


Fig. 3. Single-electron box chiptlet. (a) Schematic views of the SEB device: (top left) cross-section along the silicon channel direction and (top right) top view. A QD forms in the silicon directly under the gate electrode and is tunnel coupled to the ohmic contact. V_{rx_i} refers to the ohmic contact potential and V_{g_i} to the gate potential. The schematic elements are indicated with colored labels (bottom left). (b) Schematic of the matching network and components used in the signal-delivery lines. $V_{rx(g)DC}$ refer to quasi-static voltages and $V_{rx(g)RF}$ to radio-frequency voltages. (c) Demodulated transmitted signal as a function of gate voltage showing charge oscillations for SEB:0,1; orange and green traces, respectively.

remains static (middle panel). For $400 \text{ ms} < t < 660 \text{ ms}$, we deselect the MUX. For $t > 660 \text{ ms}$, we select MUX:1 and detect charge oscillations in SEB₁ swapping the voltage profiles on the SEB gates. We record the data while the corresponding gate voltage is being ramped up (time windows between the vertical dashed lines). Within the time resolution of our measurements which is below the inverse bandwidth of the resonators ($\sim 3 \text{ MHz}$), we do not observe any transient after the switching events.

Next, we benchmark the sensitivity of the assembly in terms of the power signal-to-noise ratio (SNR). We define the signal as the square of the voltage amplitude of a SEB oscillation as measured in the IQ plane and the noise as the square of the average standard deviation of the voltage levels at the top and bottom of the oscillation. We find a SNR of 140 at $10 \mu\text{s}$ integration time, corresponding to an integration time for SNR of 1 of 70 ns assuming a white noise profile dominated by the LNA. The result indicates that high-fidelity readout of silicon spin qubits could be achieved in timescales well below $10 \mu\text{s}$, a results that compares favorably to previous demonstrations [13], [22]. More particularly, a

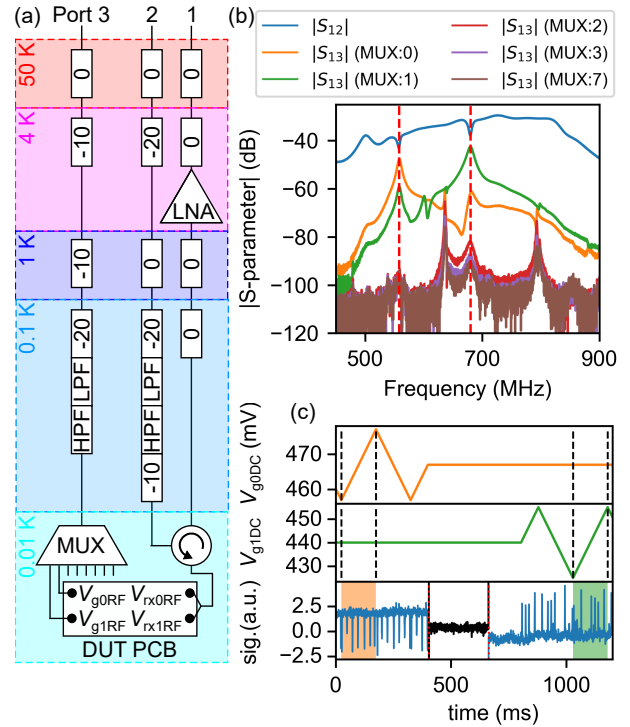


Fig. 4. Multi-module assembly and cryogenic setup. (a) Setup inside a dilution refrigerator. Rectangles indicate attenuation or low- or high-pass filtering stages. (b) S-parameter characterisation. The different traces correspond to the $|S_{ij}|$ (MUX:k) where $i(j)$ refers here to the output(input) port and k to the active MUX output channel. (c) Time-division multiplexing. Time-dependent voltage applied to gate 0 (top) and 1 (middle). Time trace of the demodulated signal (bottom).

readout fidelity well above 99%, which fulfills the readout requirements to implement a fault-tolerant quantum computer, could be achieved within a $1 \mu\text{s}$ integration time. This time is comparable to the typical surface code cycle in silicon spin qubits [15].

CONCLUSIONS

We have demonstrated a multi-module assembly for the multiplexed RF readout of silicon QD devices where all chiptlets have been manufactured using the GlobalFoundries 22FDX process. In the demonstration, we include a RF switch for the delivery of time-division multiplexed radio-frequency signals to an array of single-electron, whose transmitted signal is 50-ohm matched and amplified using a cryogenic low-noise amplifier. We benchmark the sensitivity of the assembly and find a power SNR of 140 for a readout time of $10 \mu\text{s}$, approaching state-of-the-art values [16]. We use resonators at different frequencies to demonstrate the capability of the LNA to support multiple readout channels via frequency-division multiplexing. Our results highlight the potential of CMOS technology towards the realization of a quantum computing system containing not only quantum devices but also cryogenic analog and digital electronics.

TABLE I
PERFORMANCE SUMMARY AND COMPARISON CRYO-LNA

Ref.	This Work	IMS'23 [17]	MWCL'22 [18]	JSSC'18 [19]
Technology	22-nm FDSOI CMOS	40-nm Bulk CMOS	65-nm Bulk CMOS	160-nm Bulk CMOS
Topology	Cascode CS	Inverted-based input + Noise-Canceling	Folded Cascode CS	Noise-Canceling
Meas. Temp. (K)	4	4	20	4.2
Freq. (GHz)	0.71 ~ 0.82	0.01 ~ 3	0.9 ~ 1.8	0.1 ~ 0.5
S_{21} (dB)	35	29	37.2	57
S_{11} (dB)	< -10	-11.2 ~ -8.3	< -10	-7 ~ -3
NT (K)	4.2 ~ 7.1	-	2.0 ~ 8.8	6.8 ~ 62.7
Power (mW)	36	19.4	125	91
Area (mm ²)	0.349	0.018 ^a	1 ^a	0.249 ^a

^aEstimated from figures.

TABLE II
PERFORMANCE SUMMARY AND COMPARISON CRYO-SWITCH

Ref.	This Work	Nat. Elec.'23 [20]	IMS'22 [21]
Technology	22-nm FDSOI CMOS	28-nm Bulk CMOS	22-nm FDSOI CMOS
Configuration	SP8T	SP4T	SPST
Meas. Temp. (K)	4	4	2
Freq. (GHz)	0.01 ~ 2	4 ~ 8	DC ~ 70
IL (dB)	< 1.1	< 5	< 2.3
Iso. (dB)	> 35	> 30	< 25.3
RL (dB)	> 10	8.3 ~ 11.2	> 11.5
NT (K)	< 1.1	0.15 ^a	-
Area (mm ²)	2.01	1 ^b	0.00016 ^c

^aAt 6 GHz.

^bEstimated from figures.

^cCore area only.

TABLE III
PERFORMANCE SUMMARY AND COMPARISON SEB READOUT

Ref.	This Work	Nat.'22 [22]	PRX'23 [13]
Technology	22-nm FDSOI CMOS	Si/SiGe	Si-SOI nanowire
Resonator Type	Multi-module	On-chip	Multi-module
Channel Management	TDMA	N.A.	N.A.
t_{\min} (ns)	70	1.8	170

ACKNOWLEDGMENTS

The authors acknowledge support from Jonathan Warren of Quantum Motion. M. F. G.-Z. acknowledges a UKRI Future Leaders Fellowship [MR/V023284/1].

REFERENCES

- Xue, X. et al. Quantum logic with spin qubits crossing the surface code threshold. *Nature* 601, 343–347 (2022).
- Philips, S. G. J. et al. Universal control of a six-qubit quantum processor in silicon. *Nature* 609, 919–924 (2022).
- Noiri, A. et al. Fast universal quantum gate above the fault-tolerance threshold in silicon. *Nature* 601, 338 (2022).
- Mills, A.R. et al. Two-qubit silicon quantum processor with operation fidelity exceeding 99%. *Sci. Adv.* 8, eabn5130 (2022).
- Zwerver, A. M. J. et al. Qubits made by advanced semiconductor manufacturing. *Nat. Electron.* 75, 1357584–190 (201622).
- Maurand, R. et al. CMOS silicon spin qubit. *Nat. Commun.* 5, 184–190 (2022).
- Gonzalez-Zalba, M. F. et al. Scaling silicon-based quantum computing using CMOS technology: State-of-the-art, Challenges and Perspectives. *Nat Electron* 4, 872–884 (2021).
- J. Eastoe, et al. Efficient system for bulk characterization of cryogenic cmos components. arXiv preprint arXiv:2404.11451 (2024).
- Krinner, S. et al. Engineering cryogenic setups for 100-qubit scale superconducting circuit systems. *EPJ Quantum Technol.* 6, 1–29 (2019).
- Chakraborty, W. et al. Characterization and Modeling of 22 nm FDSOI Cryogenic RF CMOS. *IEEE Journal on Exploratory Solid-State Computational Devices and Circuits* 7, 184–192 (2021).
- Paz, B. C. et al. Variability Evaluation of 28nm FD-SOI Technology at Cryogenic Temperatures down to 100mK for Quantum Computing. in 2020 IEEE Symposium on VLSI Technology 1–2 (2020).
- Ahmed, I. et al. Radio-Frequency Capacitive Gate-Based Sensing. *Phys. Rev App.* 10 014018 (2018)
- Oakes, G. A. et al. Fast High-Fidelity Single-Shot Readout of Spins in Silicon Using a Single-Electron Box. *Phys. Rev. X* 13, 011023 (2023).
- Ahmed, I. et al. Primary thermometry of a single reservoir using cyclic electron tunneling to a quantum dot. *Commun. Phys.* 1 66 (2018).
- Veldhorst, M. et al. Silicon CMOS architecture for a spin-based quantum computer. *Nat. Commun.* 8 1766 (2017).
- von Horstig, F.-E. et al. Multimodule microwave assembly for fast readout and charge-noise characterization of silicon quantum dots. *Phys. Rev. App.* 21, 044016 (2024).
- Chaubey, M. et al. A Miniature 10MHz-3GHz Sub 1-dB NF Cryogenic Inductorless Noise-Canceling Low-Noise Amplifier for Qubit Readout. in 2023 IEEE/MTT-S International Microwave Symposium - IMS 2023 668–671 (2023).
- Sheldon, A. et al. A Cryo-CMOS Low-Noise Amplifier With 2.3-to-8.5-K Noise Temperature at 20 K for Highly Integrated Radio-Astronomy Receivers. *IEEE Microwave and Wireless Components Letters* 32, 1319–1322 (2022).
- Patra, B. et al. Cryo-CMOS Circuits and Systems for Quantum Computing Applications. *IEEE Journal of Solid-State Circuits* 53, 309–321 (2018).
- Acharya, R. et al. Multiplexed superconducting qubit control at millikelvin temperatures with a low-power cryo-CMOS multiplexer. *Nat Electron* 6, 900–909 (2023).
- Nhut, T. D. et al. Cryogenic Compact mm-Wave Broadband SPST Switch in 22nm FDSOI CMOS for Monolithic Quantum Processors. in 2022 IEEE/MTT-S International Microwave Symposium - IMS 2022 168–171 (IEEE, 2022).
- Borjans, F. et al. J. R. Spin Digitizer for High-Fidelity Readout of a Cavity-Coupled Silicon Triple Quantum Dot. *Phys. Rev. Appl.* 15, 044052 (2021).